

Ultrashort Pulsed Laser-Assisted Direct Restoration of Human Enamel Using 3D Printable Biocomposite

Sarathkumar Loganathan,* Geeta Sharma, Evangelos Daskalakis, Simon Strafford, Eric Kumi Barimah, and Animesh Jha

Restorative dentistry encounters the prevalence of secondary caries due to the formation of marginal defects during tooth restoration. The present study proposes a dual-wavelength ultrashort-pulsed laser system for the direct restoration of damaged enamel to overcome marginal defects. The 2D finite element (FE) laser-ablative model is developed for studying the laser-tissue interaction. The laser-ablated cavities (rectilinear and circular) are prepared on human enamel using 800 nm, Ti:Sapphire femtosecond (fs) laser (100 fs, 1 kHz, 1 mm s⁻¹) at average laser power of 200 mW. Subsequently, the cavity is filled with 3D printed biocomposite (65 wt.% of 3D-printing resin and 35 wt.% of Ce³⁺-ion doped hydroxyapatite) and photocured using 405 nm laser. Further, the postprocessing procedure is carried out using fs laser to remove excessive filler materials and improve surface finish at sub-ablation threshold of enamel. The surface morphology, chemical compositions, mechanical and interfacial properties of restored enamel surface are evaluated. The *in vitro* evaluation study confirmed that the enamel restored with fs laser and 3D printing biocomposite is mechanically and chemically robust for withstanding oral challenges. The proposed method of restoring damaged enamel opens an opportunity for a range of precision restorative dentistry procedures including caries and tooth augmentation.

damage are the most prevalent conditions, affecting ≈100% of adults. The fabrication and surface preparation of tooth crowns is a typical procedure used in restorative dental surgery to remove carious hard tissues and construct the desired tooth geometry for restoration,^[1,2] Lasers are commonly used for tooth preparation in modern dental practice as they are minimally invasive and capable of producing a precise debris-free surface while preserving healthy tissue. Numerous medical lasers have been issued clearance by the US Food and Drug Administration for treating soft-tissue surgery (CO₂ laser–gingivectomies, aphthous ulcers. etc.), hard-tissue removal (Er:YAG laser – caries, enamel, dentin) and sterilization (Diode laser – periodontal disease, tooth whitening) in dental practice. Despite FDA approval, no laser has so far received the seal of acceptance from the American Dental Association, which is why there is an urgent need to carefully investigate the safety claims, patient benefits, and the efficiency


1. Introduction

Dentistry is currently experiencing increasing demand due to health issues, dental diseases, aesthetics, and longer lifespans. Conditions, such as acid erosion, bacterial effects, caries, and accidental tooth damage are quite common in the global population where there is an urgent need for a point-of-care solution. Untreated dental caries, periodontitis, and accidental tooth

of dental care in clinics.^[3]

The side effects of laser surgery namely, the pain, thermal damage, and mechanical cracks are directly influenced by heat diffusion and mechanical shock due to the long interaction time of the conventional lasers (pulse duration > ns). Studies on the use of ultrashort pulsed lasers (USPL) in dentistry have increased in recent decades. Niemz et al.^[4,5] demonstrated the use of USPL to prevent thermal damage on dental hard tissues. It has been claimed that the precise removal of dental hard tissue can be accomplished by multiphoton absorption with extremely high-intensity laser pulses. In the ultrashort-pulsed regime, the laser-tissue interaction time is shorter (100 fs) than the classical thermal relaxation time (few ns) thus the material ablation is completed before heat diffusion to achieve “cold ablation.” Hence, the collateral damage to the adjacent tissue and necrosis can be minimized using suitable USPL,^[3,6] Petrov et al.^[1] created a well-defined precise rectangular cavity on dental tissues without any detrimental thermal effects and material phase changes. Wang et al.^[7] demonstrated the automatic tooth crown preparation by controlling the laser beam with a robotic arm. Recent studies have reported that the debris-free ablation characteristics of the femtosecond (fs) laser-irradiated surface enhance the

S. Loganathan, G. Sharma, E. Daskalakis, S. Strafford, E. Kumi Barimah, A. Jha
School of Chemical and Process Engineering
University of Leeds
Woodhouse, Leeds LS29JT, UK
E-mail: s.loganathan@leeds.ac.uk

 The ORCID identification number(s) for the author(s) of this article can be found under <https://doi.org/10.1002/admt.202401362>

© 2025 The Author(s). Advanced Materials Technologies published by Wiley-VCH GmbH. This is an open access article under the terms of the [Creative Commons Attribution](https://creativecommons.org/licenses/by/4.0/) License, which permits use, distribution and reproduction in any medium, provided the original work is properly cited.

DOI: 10.1002/admt.202401362

binding strength of resin composites,^[1,8] However, precise material removal due to cold ablation can only be achieved by controlling the laser fluence between slightly above the laser ablation threshold and a well-defined ablation region. Uncontrolled laser processing conditions (laser fluence, scanning speed, and repetition rate) can lead to excess tissue removal and heat accumulation (shielding effect) by repetitive high-intensity pulse incidence.^[1,6] Therefore, it is essential to determine the optimal laser processing condition to ensure a controlled cold ablation process for precise tooth preparation. A variety of computational models have been developed so far to simulate thermal response due to laser-tissue interaction using the Fourier heat conduction equation (FHCE) and bio-heat equation.^[3,9] However, simulation of the laser ablation profile along with thermal response has potential benefits in operating the laser beam for ensuring higher accuracy to preserve healthier tissues. With the rapid development of artificial intelligence (AI), USPL technologies, computer-aided design, and manufacturing, it is expected that the USPL applications for dental restoration may be implemented in clinical use shortly.

In tooth filling, photo-curable biocomposites are widely used due to their strong chemical stability, mechanical strength, and aesthetic quality in the oral environment. The biocomposites are comprised of inorganic filler materials (quartz, silica, and oxides of zirconium, strontium, and titanium or zinc ceramic powder) reinforced in the photo-curable resin matrix (methyl acrylate monomers such as bis-GMA, UDMA, HEMA, and TEGDMA).^[10,11] The chemical composition differences between the biocomposites and natural enamel result in poor adherence to the prepared cavity wall, which may contribute to increased pulpal inflammation, staining, subsequent caries, and postoperative sensitivity. To address these issues, hydroxyapatite (HAp) based fillers are extensively used in dentistry and orthopaedics since they are chemically comparable to teeth and bones. Moreover, the substitution of Ca^{2+} ions in the HAp lattice with other elements (Ag^+ , Zn^{2+} , $Ce^{3+/4+}$, Si^{4+} , Sr^{2+} , etc.) can improve its solubility, wear resistance, thermal stability, and antibacterial properties. Despite other trace elements, Ce^{3+} -doped HAp acts as an antimicrobial agent with high thermal stability, it plays a vital role in the prevention of future caries development and reduces enamel demineralization.^[12] On the other hand, methacrylate-based photo-curable resins are recognized (ISO 10 993) for their biocompatible properties for 3D-printing implants and dental restoration.^[13] Xia et al.^[14] demonstrated the restoration of anterior dentition using an externally 3D-printed template and photocurable resin composites to achieve improved aesthetic appearance. With the development of 3D printing technology for medical devices, there is an increase in demand for new biocompatible materials that fulfill the functional requirements of natural enamel. Hence, it is essential to use HAp-based filler materials in direct tooth restoration.

The present study aimed to directly restore a damaged enamel using a structurally compatible 3D printing bio-composite. A dual-wavelength USPL system was adapted for precise cavity preparation and filling. A novel 2D FEM laser ablative model was developed for surface preparation thus the collateral damage of healthier tissue is minimized. An integrated dual-wavelength laser enables direct cavity prepara-

tion and restoration on human enamel using a 3D-printing bio-composite. The proposed technique for restoring damaged enamel with a dual-wavelength USPL system as a surgical tool is viable and has a promising future in dental applications.

2. Experimental Section

2.1. Tooth Sample Preparation

The properly sterilized human enamel samples were obtained from the dental hospital. The top layer of the tooth was grounded to make a flat enamel and appropriate measures were taken to prevent excessive wear of the enamel surface. The flat enamel surface was sectioned out transversely into 2–3 mm thickness from the teeth with a high-speed diamond cutter and polished using silicon carbide polishing cloth (#1200 grit size) in the presence of water as coolant. Further, the samples were ultrasonicated in distilled water to remove polishing debris and kept in the artificial saline to maintain the artificial oral environment.

2.2. Preparation of Filler Material

HAp nanoparticles doped with 3% Ce^{3+} -ion were synthesized using the sol-gel technique as reported in earlier work.^[15] The dental filling was prepared by homogeneous mixing of 65 wt.% of biocompatible 3D printing photocurable resin (FormLabs/Dental Clear LT/SLA/ISO 10 993) with 35 wt.% of Ce^{3+} -doped HAp nanoparticles.

2.3. Laser Processing for Cavity Preparation, Photocuring, and Postprocessing of Filler Material

The dental cavity was prepared using 800 nm, 100 fs, 1 kHz Ti: Sapphire fs laser. The laser system can deliver a maximum average power of 1 W with Gaussian spatial distributions, and it can be regulated by a variable attenuator. The laser irradiation on dental hard tissues was performed using a 6.4 mm focal lens and the beam was focused perpendicular to the enamel surface with the help of an automatic focusing CCD device (**Figure 1**). The dental enamel of ≈ 1.2 mm thickness was loaded on a high precision, CNC-controlled XYZ table with 100 nm resolution. The grooves were made on the enamel surface at various laser powers (0.1 to 0.6 W) by adopting a single-line scanning (1 mm s^{-1}) method to determine the optimum laser power.

The rectangular (1 mm x 1 mm) and circular cavity (diameter of 1 mm) were prepared on the enamel surface at the average laser power of 0.2 W with a scanning line overlap of 10 μm . The double scanning layer method was used to achieve the cavities with a depth of $\approx 60 \mu\text{m}$. The laser-machined debris on the enamel surface was removed by ultrasonic cleaning in the presence of distilled water and air-dried. Further, the cavity was filled with the slurry and photocured using a 405 nm UV-diode laser. The fs-laser postprocessing experiment was carried out on restored dental enamel to remove excess filler material. The average laser power was maintained within the sub-ablation threshold of enamel (10 mW) to avoid enamel ablation during the postprocessing procedure.

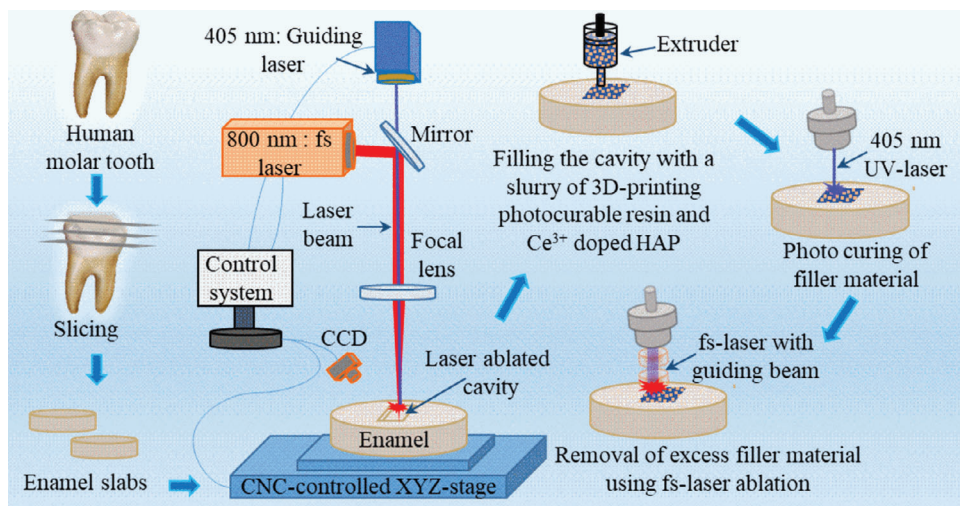


Figure 1. Laser-based tooth preparation and direct filling technique on human enamel.

2.4. Characterization

The surface morphology of the ablated dental enamel surface was analyzed using a confocal laser-scanning microscope (Carl Zeiss LSM800 Mat CLSM) and SEM (Hitachi TM3030Plus SEM with EDX). Each measurement was repeated three times to confirm the repeatability of the dimensions (depth and width) and surface roughness evaluated on the ablated surface. The interfacial bonding between the enamel and the biocomposite was studied using cross-sectional SEM and micro-CT scan (SkyScan 1172) with a scanning resolution of 1 μm . The Vickers micro-hardness (BUEHLER Wilson Hardness tester) of the photocured biocomposite was examined for available loads of 0.1, 0.2, 0.3, 0.5, 1 and 2 kg, to demonstrate that it is independent of load. The diamond micro-intender was pressed against the sample for 10 seconds. The Vickers micro-hardness was calculated using equation ($HV = 1.854 F/D^2$), where F is the kilogram-force (N) and D is the average diagonal length (m). The (D) was extrapolated from the diagonals of the indentation spot using *Image J* software. The chemical composition of the ablated cavity and filled surface was analyzed using energy dispersive spectroscopy (EDS) and Raman spectroscopy.

3. Computational Model for Laser Ablation

In an USPL, the two-step energy transfer process takes place. The photon energy is first transferred to electrons by photon-electron coupling and then to the phonon by electron-phonon coupling.

The electron and phonon may not reach the thermal equilibrium at the early time of laser-material interaction because the pulse duration (<10 ps) is shorter than the thermal relaxation time (>10 ps). Hence, numerous two-temperature model (TTM) was proposed to model ultrafast thermal profiles in metals, semiconductors, and dielectrics. However, the TTM is not necessary for modeling thermal response in dental tissues heated by a train of fs pulses that have a longer pulse separation time (>few ns) between two consecutive pulses.^[3] Hence, the classical FHCE can be used to model thermal response in dental hard tissues without compromising accuracy. Furthermore, this alternative method

can also reduce the enormous computational time because of the tiny time steps (<ps) necessary in a TTM.

In this study, the 2D-Cartesian model was developed using COMSOL Multiphysics to predict laser ablation profile on the thin layer of human enamel ($\approx 100 \mu\text{m}$) for different laser fluence at a constant repetition rate (1 kHz) and scanning speed (1 mm s^{-1}). The general 2D FHCE for multi-pulse laser heating at the x - y cross-sectional plane (Figure 2a) is given as,^[3,16]

$$k \left[\left(\frac{\partial^2 T}{\partial x^2} \right) + \left(\frac{\partial^2 T}{\partial y^2} \right) \right] + \sum_{i=1}^n S_i = \rho C_p \frac{\partial T}{\partial t} \quad (1)$$

where k is thermal conductivity (W/mK), T is temperature (K), ρ is mass density (kg/m^3), C_p is specific heat capacity (J/kgK) at constant pressure and S_i is the laser heat flux generated from each pulse i . The Gaussian spatial distribution of laser pulse can be described as the analytical function of x and t in spatial and temporal coordinates, respectively,^[3,17]

$$S_i(x, y, t) = \alpha (1 - R) \frac{F}{t_p} \cdot e^{-\frac{(x-x_0)^2}{2\sigma^2}} \cdot e^{-2.77 \left(\frac{t-t_i}{t_p} \right)^2} \cdot e^{-\alpha y} \quad (2)$$

in which α is the absorption coefficient, R is surface reflectivity, F is the laser fluence, t_p is the pulse width, x_0 is the position of the laser beam spot in Cartesian coordinates, σ is the standard deviation of the Gaussian laser beam and t_i is a time of peak power at i^{th} laser pulse. The boundaries 1, 2, and 4 in Figure 2b are subjected to convection heat loss as Equation (3), and boundary 3 is subject to thermal insulation (Equation 4).

$$-k \frac{\partial T}{\partial x} = h_c (T - T_a) \quad (3)$$

$$\frac{\partial T}{\partial y} = 0 \quad (4)$$

where h_c is the convective heat transfer coefficient ($\text{W/m}^2\text{K}$) and T_a is ambient air temperature (K). The thermophysical properties

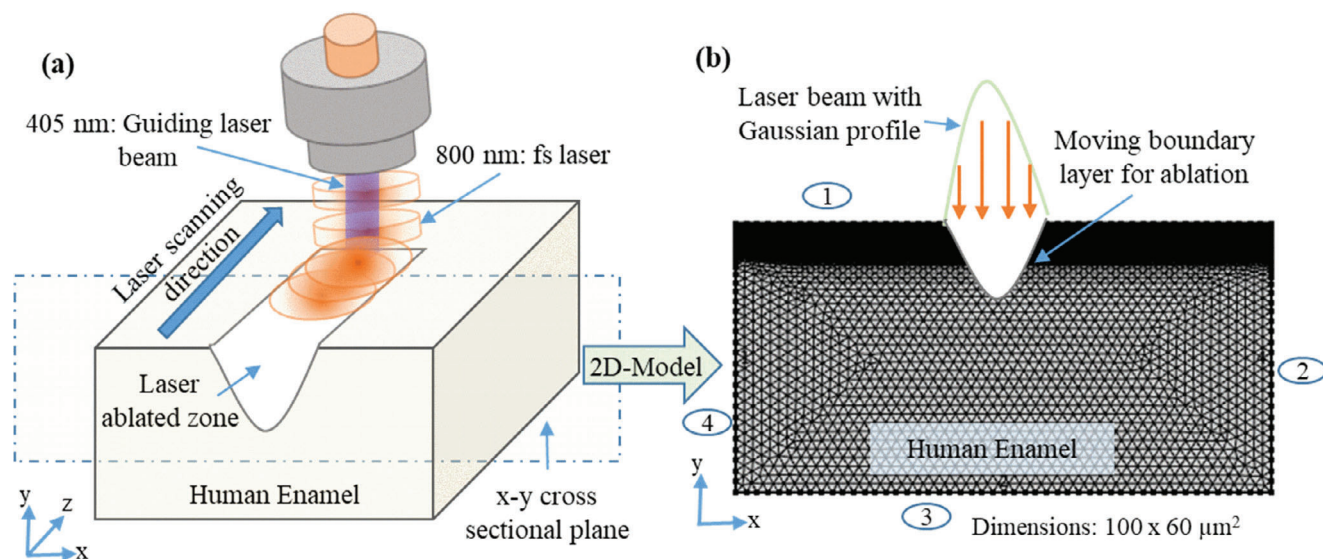


Figure 2. a) Schematic of laser-ablated groove with x-y cut section on human enamel and b) 2D geometry considered for FE model at x-y cross-sectional plane in cartesian coordinates.

of the dental hard tissue and laser input parameters are given in **Table 1**.

In fs-laser, the material starts to ablate when the laser-matter interaction region reaches the evaporation temperature by forming a gaseous phase. To compute the change in the shape of ablated geometry due to direct evaporation, the moving mesh approach was adopted by assuming that the material removal occurs when the target material reaches the evaporation temperature (T_v) and removing the geometric elements that reach the evaporation temperature of enamel (2273 K). In this model, the laser-ablated cavity formed during evaporation is expressed by the convective heat flux given in Equation (5):

$$\varphi_{\text{vap}} = h_a (T - T_v) \quad (5)$$

where φ_{vap} is the ablative heat flux ($\text{W}/\text{m}^2\text{K}$) and h_a is a numerical parameter. The top surface (boundary 1) is subjected to move freely to accommodate the geometrical change due to the evaporation. The normal mesh velocity (v_n) on the moving boundary layer at the solid-gas interface is expressed as Equation (6).

$$v_n = \varphi_{\text{vap}} / (\rho \cdot L_v) \quad (6)$$

Table 1. Thermophysical properties of human enamel.

Properties	Human Enamel	Refs.
Thermal conductivity (W/mK)	0.97	[3, 19]
Specific heat capacity ($\text{J}/\text{kg}\cdot\text{K}$)	711.28	[3, 19]
Density (kg/m^3)	2800	[3]
Convective heat transfer coefficient ($\text{W}/\text{m}^2\text{K}$)	10	[3]
Evaporation Temperature (K)	2273	[20]
Melting Temperature (K)	1400	[21]
Heat of evaporation (J/kg)	4000×10^3	[20, 21]
Absorption coefficient (m^{-1})	0.0084	[3]

where L_v is the latent heat of vaporization (J/kg).^[18]

4. Results and Discussion

4.1. Modeling Results

The major challenge clinicians may face during laser-based tooth preparation techniques is to predict the optimal laser processing conditions for safe operation. Instead of conducting several experiments, the computational model may be used as a guiding tool for estimating the laser energy penetration depth and crater dimension based on the in situ measurements of the temperature profile. The present model is simulated at a laser beam diameter ($2\omega_0$) of $12.4 \mu\text{m}$ calculated using Equation (7)^[22] by considering the laser beam quality factor (M^2) = 1.9, laser beam wavelength (λ) = 800 nm, focal distance (f_o) = 6.4 mm and the diameter of the laser beam (D) at the lens = 1 mm.

$$2\omega_0 = 4M^2 \lambda f_o / (\pi D) \quad (7)$$

Using the laser beam diameter in Equation (7), the effective number of pulses at the point of focus (f) at a given scanning speed (v) in Figure 2a may be simulated at the instantaneous time by using the effective number of pulses (N_{eff}) estimated from Equation (8).^[6]

$$N_{\text{eff}} = \sqrt{\frac{\pi}{2}} \cdot \frac{\omega_0 f}{v} \quad (8)$$

The value of N_{eff} is calculated as ≈ 16 for the focused laser beam diameter of $12.4 \mu\text{m}$, laser scanning speed (v) of 1 mm s^{-1} and repetition rate (f) of 1 kHz.

The laser-tissue interaction occurs within the confined volume of $\approx 100 \mu\text{m}^3$ for an ultrashort time scale ($< \text{ps}$). This localized nature increases the surface temperature ($> 18\,000 \text{ K}$) tremendously in a short time. However, the tissue starts to ablate

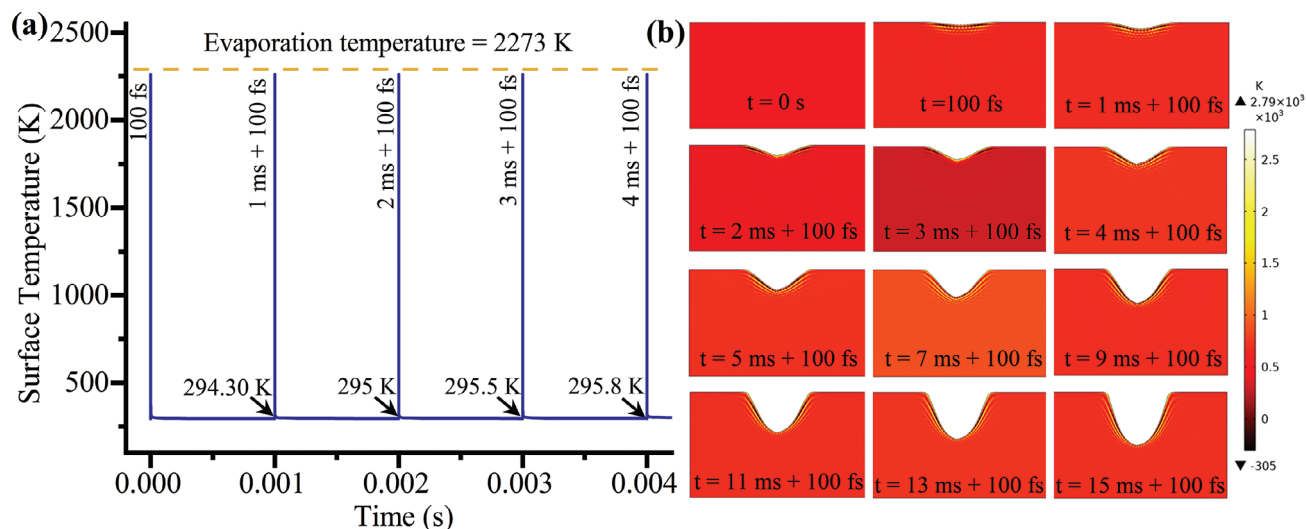


Figure 3. a) Surface temperature predicted on the tooth enamel for the train of laser pulses based on the FE model at the average power of 200 mW and repetition rate of 1 kHz. b) The change in the laser ablation profile corresponds to different pulse numbers.

by directly forming a gaseous phase once it reaches the threshold where the molecular bonds begin to break and volatilize. Consequently, tissue removal occurs at the surface, and the temperature rise is regulated by molecular bond breakage and ablation since most of the heat energy is carried away by the ablated particles (as shown in **Figure 3a,b**). The laser ablation profile follows the spatial nature of Gaussian energy distribution, resulting in higher material removal at the center compared to the edge of the beam profile. **Figure 3a,b** shows the surface temperature and ablation profile of dental enamel for the train of laser pulses at the average laser power of 200 mW. The average net rise in temperature between two consecutive pulses is ≈ 0.5 K. The temperature at the initial phase of laser pulse interaction was extremely high for each pulse due to the non-equilibrium temperature between electron and phonon in the sub-picosecond time scale. However, the tissue reaches thermal equilibrium (294.30 K) before the initiation of successive pulses because of the extended pulse separation time (0.001 s). The final temperature of each pulse acts as an initial temperature for the upcoming laser pulse (**Figure 3a**). Likewise, the surface of the ablated groove created by each pulse acts as a fresh surface for the next pulse (**Figure 3b**).

The predicted ablation profile (**Figure 4a,c**) of the moving laser source was compared with the experimentally obtained cross-sectional profile of the laser-ablated groove (**Figure 4b,d**) for different laser powers (100 and 200 mW). **Figure 4** illustrates that the 2D simulation of laser ablation is in good agreement with the experimental results, despite some minor deviations. This variation in the ablation profile might be the change in the laser absorptivity when the cavity is formed. Once the groove is formed during the initial few laser pulses, the ablated particle from the groove surface starts to interact with the upcoming laser pulses (shielding effect) which changes the laser absorptivity drastically. The variation in laser absorptivity was not incorporated in this model which could account for the slight deviation in the ablation profile. The good apparent correlation between the modeling and experimental results suggests that the 2D laser abla-

tive model might be a useful tool for performing precise dental surgery.

4.2. Femtosecond Laser Processing for Determining Ablation Threshold, Ablation Rate, and Ablation Efficiency

The ability to generate a debris-free cavity surface is one of the essential characteristics of the tooth preparation method for enhancing the bond strength of the filler material.

In a pulsed laser-based tooth preparation technique, the laser must be operated at the well-defined ablated region to achieve a debris-free surface. Hence, the laser ablation study was conducted to identify the well-ablated region on dental enamel by adapting a single-line scanning technique at different laser powers (0.1 to 0.6 W, 1 mm s^{-1} , 1 kHz). The dimension and surface roughness of the ablated grooves on irradiated enamel were measured using a confocal image (**Figure 5a**). The ablation threshold and efficiency on the enamel surface were calculated using the ablation width square method adopted by Sarathkumar et al.^[6] **Figure 5c** shows the linear fit ($R^2 = 0.96$) of the squared ablation width plotted against the logarithmic value of laser pulse energy and it follows a positive correlation. The laser ablation threshold fluence on human enamel is calculated as 4.08 J cm^{-2} which is obtained from the slope and intercept of the empirical relation arrived from the linear fit. The laser ablation efficiency varies from 3.95 to $2.86 \text{ mm}^3 \text{ J}^{-1}$ for different laser powers (**Figure 5d**). The ablation efficiency is increased up to 200 μJ and it starts to decline/saturate after that at the higher laser powers due to the shielding effect as mentioned earlier. The maximum laser ablation efficiency ($4.13 \text{ mm}^3 \text{ J}^{-1}$) was observed at pulse energy/average laser power of 200 μJ /0.2 mW (**Figure 5d**). Likewise, it is also noticed (**Figure 5a**) that the value of surface roughness ($0.83 \mu\text{m}$) is minimal at the average laser power of 0.2 W which is measured at the bottom line of the ablated groove. The SEM image shows no thermal damage on the ablated grooves reaffirming the confocal data (**Figure 5b**). Thus,

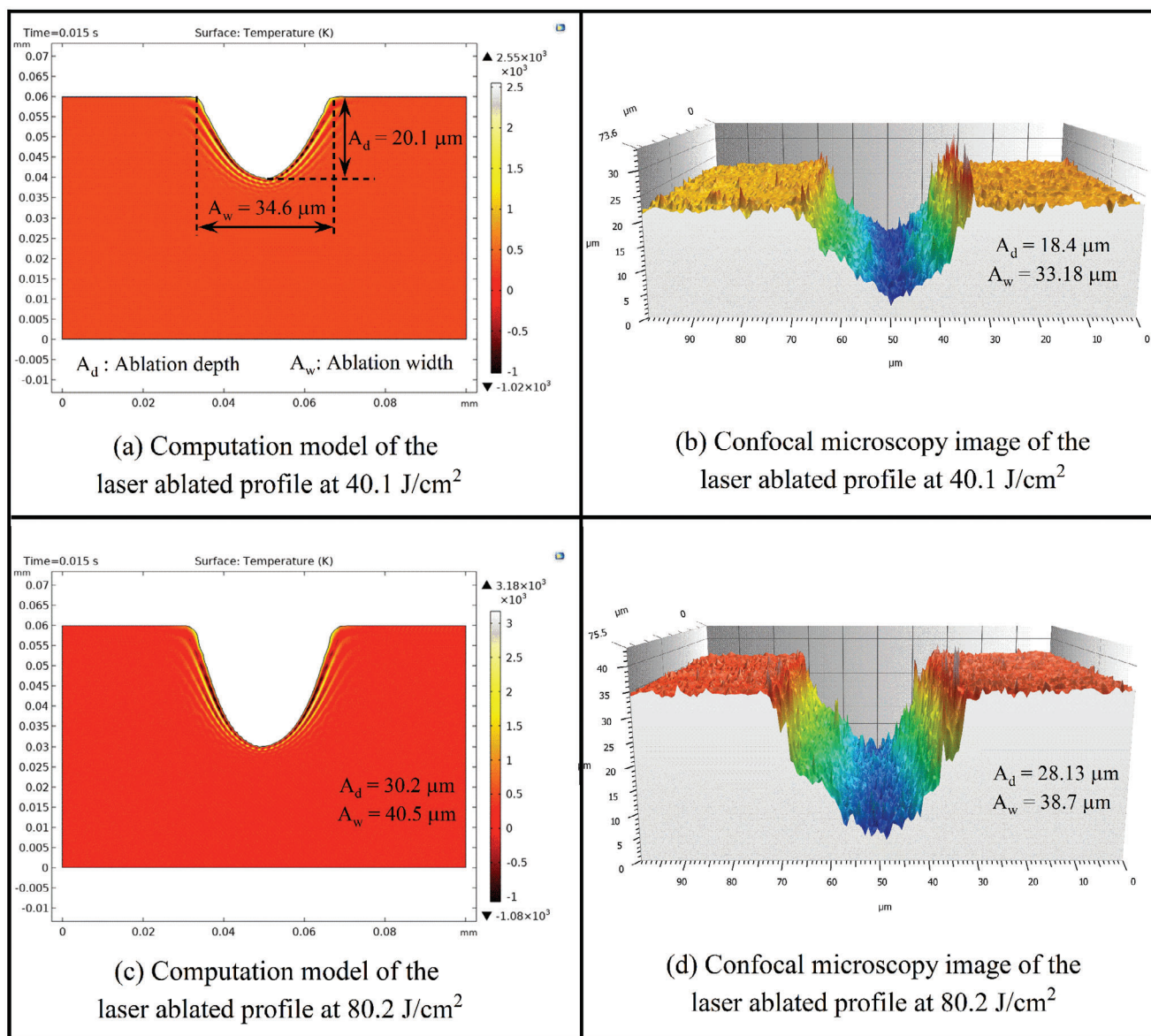


Figure 4. Comparison of FE model with experimental results. The predicted laser ablation profile using the FE model at the laser fluence of a) 40.1 J cm^{-2} and c) 80.2 J cm^{-2} . The experimentally obtained cross-sectional profile of the laser-ablated groove using a confocal microscope at the laser fluence of b) 40.1 J cm^{-2} and d) 80.2 J cm^{-2} .

the laser ablation study proposes that the debris-free ablated cavity on dental enamel may be possible to prepare at an average laser power of 0.2 W based on ablation efficiency and surface roughness.

4.3. Cavity Preparation on Dental Hard Tissue

The laser irradiation effects on healthier tissues can be reduced by controlled scanning of the laser beam over the dental hard tissue instead of directing the laser beam in only one position. In the case of the stationary position of the laser beam onto the target tissue, the number of pulses accumulating on the particular region is increasing which results in heat accumulation similar to deep

drilling. Thus, the rectilinear ($1 \times 1 \text{ mm}^2$) and circular shaped (1 mm diameter) cavities were created using a laser scan head and CNC-controlled XYZ stage as elaborated in Section 2.3. The dimension and surface roughness of the ablated cavities were analyzed using a CLSM image (Figure 6a,b). The primary inspection of all ablated zones showed no shape distortion, micro-cracks, or collateral damages in either rectilinear or circular cavities. The depth of rectilinear (61.4 μm) and circular cavities (59.8 μm) are almost comparable with slight variation. Also, the surface roughness of the rectilinear cavity (0.486 μm) is better than the circular one (0.592 μm). These variations may be attributed to changes in the interaction of laser-ablated particles with upcoming laser beams while machining two different geometries. The locus of the laser beam spot (relative motion to the target) is entirely

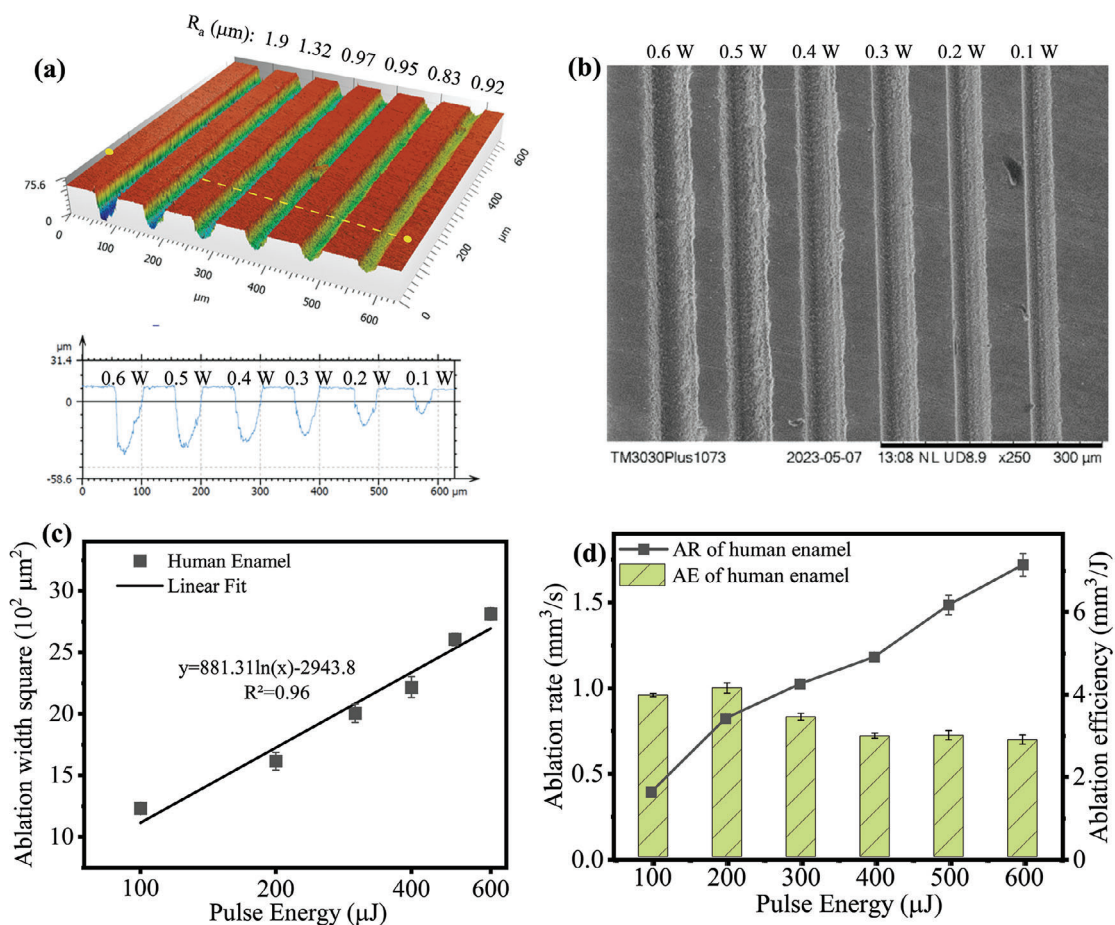


Figure 5. a) Confocal microscopy image of laser ablated groove at various laser powers on human enamel. b) SEM analysis of laser ablated groove on human enamel. c) Ablation behavior of fs-laser irradiated on dental enamel. The squared ablation width is plotted against the laser pulse energy. The symbol and solid line denote the experimental data and linear fit, respectively. d) The laser ablation rate (left y-axis) and ablation efficiency (right y-axis) are plotted as a function of laser pulse energy.

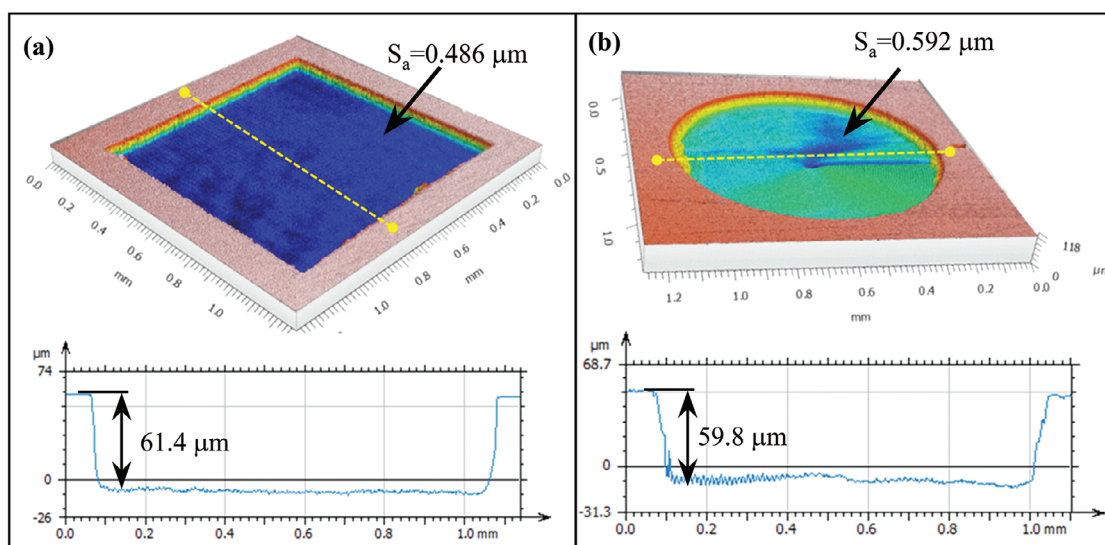


Figure 6. Confocal microscopy image of the laser-ablated cavity on human enamel at the average laser power of 0.2 W and scanning speed of 1 mm s^{-1} with $10 \mu\text{m}$ overlap. a) Rectilinear and b) Circular cavity.

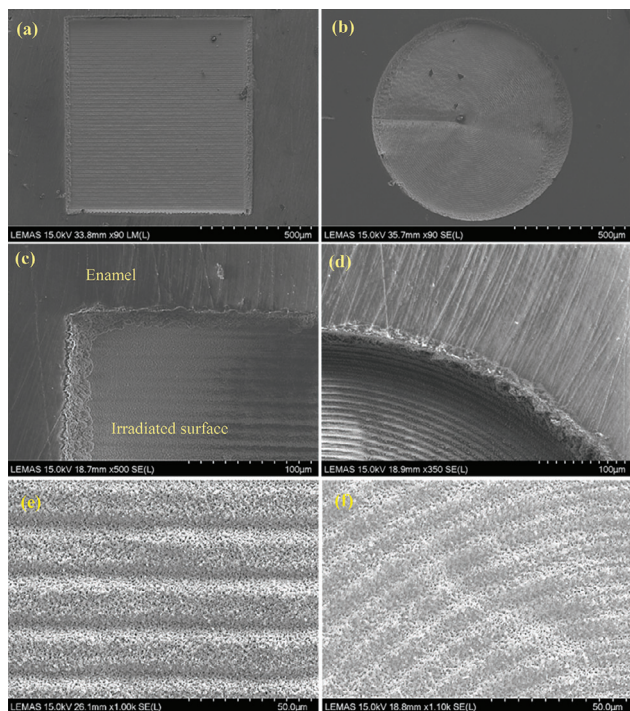


Figure 7. Surface morphology analysis of rectilinear (left) and circular (right) laser-ablated cavity. a,b) SEM images of ablated cavities. c,d) Cavity edge between intact and irradiated enamel. e,f) Surface morphological changes in rectilinear and circular cavities on enamel with advantageous debris-free surface.

different for machining a circular cavity that creates a swirling effect within ablated particles leading to a higher shielding effect than a rectilinear one. As a result, the formation of a redeposited layer is more pronounced in the circular cavity impacting ablation depth. However, this redeposited layer is removed during the ultrasonication process.

The surface morphology and microstructural properties of ablated enamel were investigated using SEM (Figure 7). The irradiated zones in both rectilinear and circular cavities were homogeneously ablated and thermal damage was not present around the cavities reaffirming the confocal data. The ablated cavities featured precise vertical walls and edges that are typical for fs laser interaction with tissue (Figure 7a,b). The corners are free from deep pockets that arise when scanning the meander design. Also, the high-magnification SEM image of the edge between the untreated surface and ablated enamel (Figure 7c,d) showed no melting, discolorations, debris, or microcracks due to laser irradiation on the enamel. The ablated enamel revealed the morphological changes as seen in Figure 7e,f. In contrast to a smooth untreated surface, the laser-ablated surface yielded high surface roughness, and this can be optimized by adjusting the scanning line overlap. The previous studies,^[1,23] found that an increase in surface roughness has a significant impact on the bonding of filler material to the dental cavity. Hence, the ablated dental cavity with high micro-roughness might be beneficial because it provides an extensive surface area for enhanced bonding with the cavity.

The change in molecular structure and chemical composition of dental enamel were investigated using Raman spectroscopy.

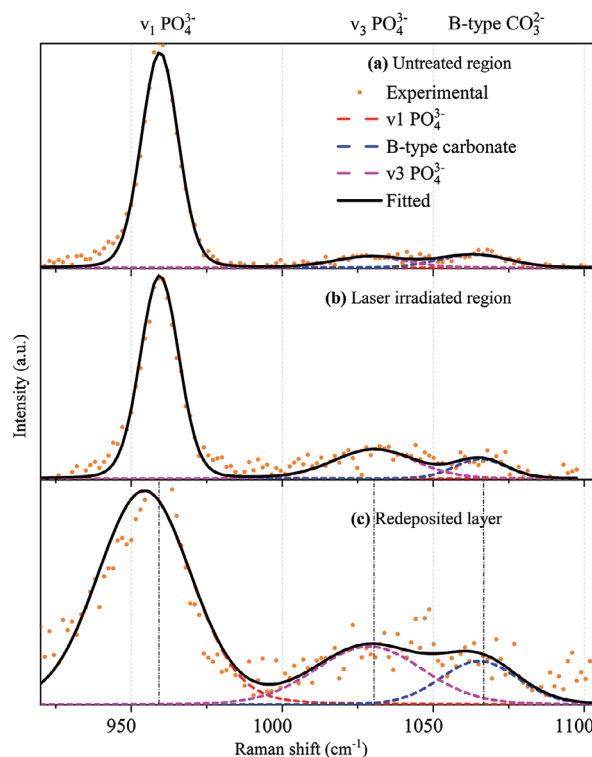


Figure 8. Raman spectra of human enamel irradiated at an average laser power of 200 mW. a) untreated, b) laser irradiated, and c) redeposited layer.

The obtained Raman data are normalized by using *fityk* software (open access). The Raman spectra of enamel samples were evaluated to study the chemical compositional variation before and after irradiation. Raman spectroscopy of intact human enamel shows the characteristic peaks of carbonated HAp dominating the spectral range of 940–1100 cm^{-1} (in Figure 8). The main characteristics peak at 960 and 1040 cm^{-1} corresponding to ν_1 and ν_3 bands in the phosphate group (PO_4^{3-}) of HAp. The C–O bond in the B-type carbonate (CO_3^{2-}) group was presented at 1065 cm^{-1} . Although the proteins are not abundant in enamel, they are crucial for regulating the nucleation, development, and organization of HAp crystals. The Raman spectra reaffirmed that the enamel mainly enriched with inorganic compounds due to the low intensity of the CO_3^{2-} group was found at 1065 cm^{-1} . The spectra of human enamel after the laser irradiation preserved the characteristic features of inorganic HAp (PO_4^{3-} group, Figure 8b).

The characteristic spectra of HAp (960, 1040, and 1065 cm^{-1} in Figure 8b) were more pronounced on the laser-irradiated (inside the cavity) surface which may be due to fresh exposure of enamel surface after laser ablation and the effect of removing the surface contamination. However, the relative peak intensity of the PO_4^{3-} group was decreasing on the cavity wall showing the formation of amorphous calcium phosphate (ACP) (Figure 8c) that may be attributed to the leftover ablation debris or redeposited layer, which may be removed after ultrasonication before tooth filling. In essence, Raman spectroscopy of HAp revealed no phase changes which means no thermal damage was attained with the laser-based cavity preparation.

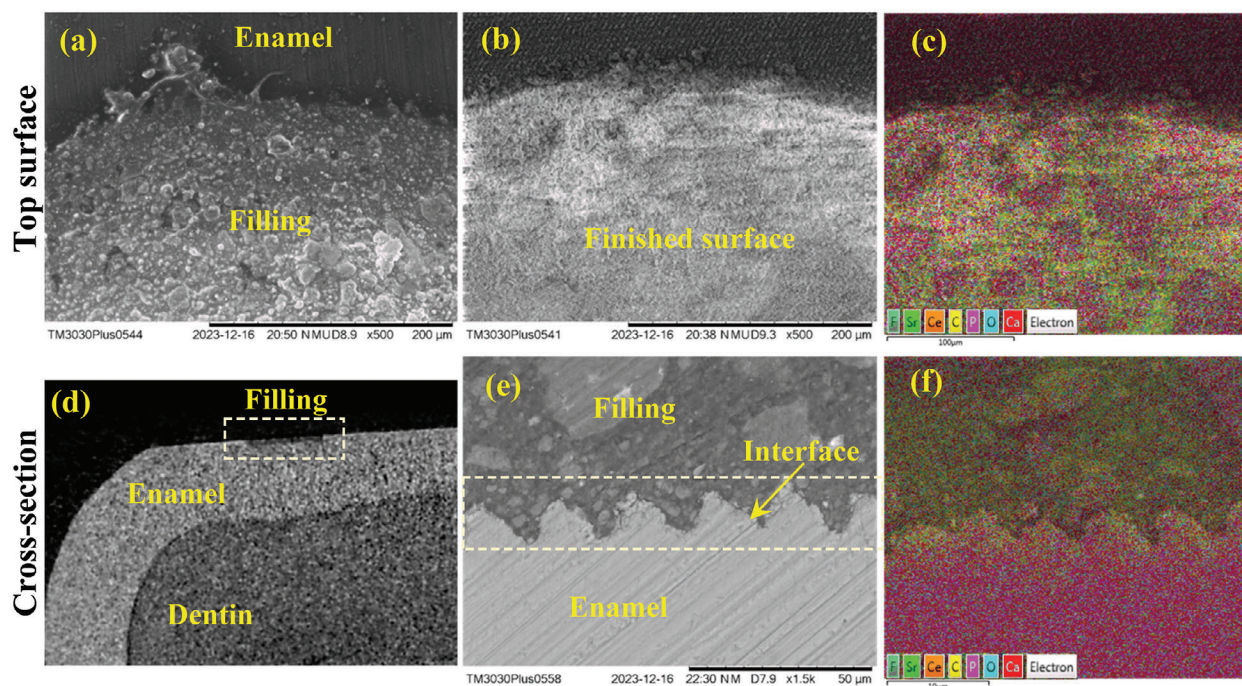


Figure 9. a) SEM image of the dental cavity filled with photocurable resin composites after UV curing. b) Removal of excess filler material and surface finish using fs laser ablation. The interfacial characteristics of enamel and filler material were analyzed using d) CT-Scan and e) Cross-sectional SEM images. c,f) The EDS mapping shows the key elemental composition of inorganic materials distributed in the resin matrix.

4.4. Tooth Filling

The laser-ablated dental cavity on human enamel was filled with 3D printing photocurable biocomposites (refer to Section 2.2) using an extruder. The filler material was photocured using a 405 nm UV laser with an average power of 150 mW. The

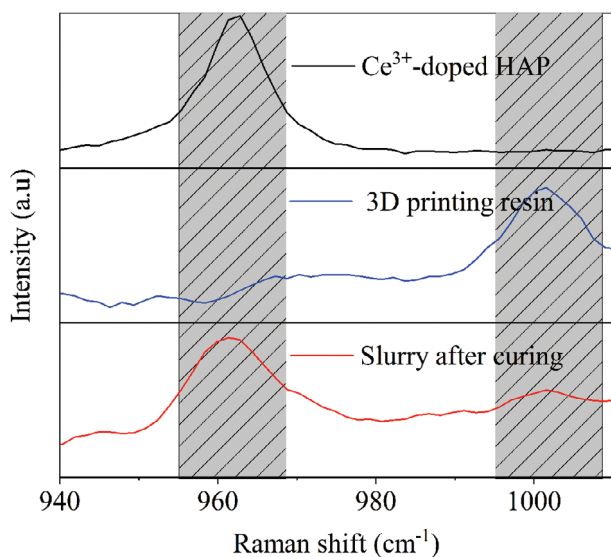


Figure 10. The comparison between the characteristics Raman spectra of inorganic minerals, 3D printing resin, and tooth fillings (slurry) after UV curing.

photocured filler material on the laser-ablated cavity shows a homogeneous, compact, and densified layer (**Figure 9a**). The excessive dental fillings spread over the enamel surface were removed using an fs laser during the post-processing procedure. The major challenge clinicians can face during tooth restoration is removing the excess filler material as it needs precise removal to match the tooth profile without damaging the natural dental tissues. **Figure 9b** shows an SEM image of the dental filling after the post-processing using fs-laser. To preserve the natural enamel, the average power of the fs laser (10 mW) is maintained at the sub-ablation threshold of enamel for the entire surface finishing process. As a result, the excessive dental fillings were removed while preserving the natural enamel (**Figure 9b**). The micro roughness of the finished surface is measured as 0.174 μm . No microcracks, or thermal damage were observed on the laser-finished surface.

The cross-sectional SEM and CT-scan images were taken to analyze the morphology and any micro-cracks at the interfacial layer (**Figure 9d,e**). The EDS mapping (**Figure 9c,f**) shows the distribution of key elements in the resin matrix after laser curing and enables to identification of the interfacial region between enamel and filler material. The concentration of Ce^{3+} doped HAP mineral is evenly distributed in the resin matrix providing the adhesion at the interface. The UV-treated region was photocured homogeneously, compact and micro-cracks were not present around the interfacial zone and enamel. The underlying enamel and photocured layer have no significant micro-cracks attributed to the overexposure of UV laser. This was supported by the high-resolution cross-sectional SEM and EDX (**Figure 9c,d**).

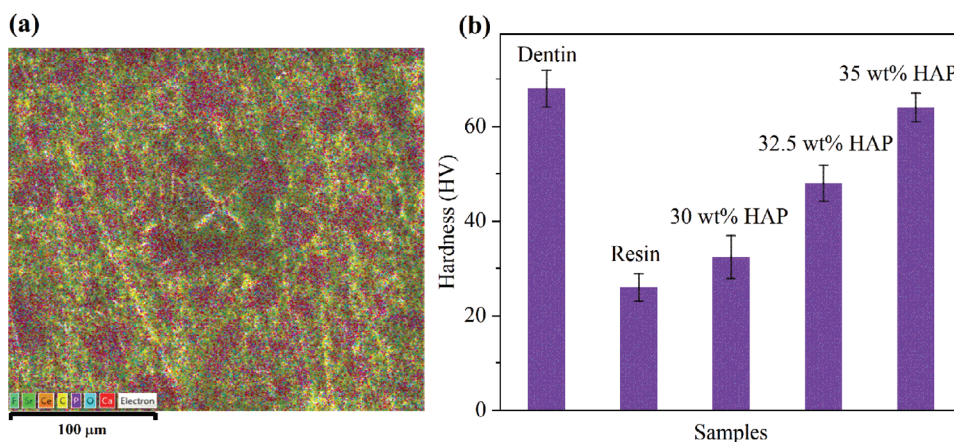


Figure 11. a) EDS mapping of dental fillings after Vickers hardness test. b) The hardness values are plotted against the varying concentrations of inorganic minerals present in the dental fillings and dentin.

The chemical composition of photocurable 3D printing resin is analyzed using Raman spectra as shown in **Figure 10**. The Raman spectra for inorganic minerals (**Figure 10a**) show a pronounced band at 960–970 cm^{-1} due to the symmetric stretch vibration of PO_4^{3-} (ν_1) in HAp.^[24] The band between 990 and 1014 cm^{-1} (**Figure 10b**) may correspond to the rocking vibration of the ν (O–C) bond in methacrylic acid ester.^[25,26] The spectra of photocured dental fillings (**Figure 10c**) confirm the presence of HAp mineral and methacrylic acid ester resin post-photocuring. The retention of HAp characteristics in the photocured composite indicates that the polymerization of the resin does not alter the structure of inorganic minerals.

The Vickers microhardness of photocured fillings is presented and compared with the hardness of natural dentin (**Figure 11**). The average diagonal length was measured using the “Image J” software.^[27] A range of loads was tested (200, 300, 500 g) to verify that the Vickers microhardness of the photocured fillings is independent of load. In **Figure 11**, the indentation spot generated by a 300 g load on the 35 wt.% of Ce^{3+} doped HAp filling demonstrated higher Vickers microhardness (64 ± 3 HV) compared to pure resin filling (26 ± 2.9 HV). Among the four tested Ce^{3+} doped HAp fillings, 35 wt.% of Ce^{3+} doped HAp exhibited Vickers microhardness comparable to the natural dentin (68 ± 3.9 HV) due to its higher mineral content (535 HV).^[28] Increasing the mineral content past 35 wt.% resulted in particle agglomeration and insufficient particle wetting by the resin, which compromised the flowability of the bio-composite during the dental restoration process.

The cavity preparation as well as direct restoration of dental enamel have been proposed using USPL and 3D printable biocomposite. In our previous study,^[6] we developed a mathematical model to predict the laser ablation profile on dental hard tissues, aimed at preventing excessive tissue removal. The mathematical model was confined to predicting the ablation profile and provides no information on thermal response. With the conjecture that the laser ablative 2D FE model could perform this task, the current study was aimed at modeling both the laser ablation profile and thermal response for preserving the healthy tissues. Dental surgery and restoration of damaged teeth have been

performed so far by conventional lasers (pulse duration > ns) those ablation rates are comparable to mechanical drills. However, the precision of these lasers is questionable due to their undesired thermo-mechanical effects. Their ablation mechanism is primarily based on the photo disruptive effect where the absorption of laser energy on hard tissue converts the water (bounded within the enamel) into superheated steam leading to the formation of a high-pressure shock wave. As a result, the surrounding hard tissue is blasted away and the tooth particles are removed as part of ablation. Thus, the USPL is needed for precise dental treatment as the replacement of conventional lasers. The present study demonstrated the application of fs-laser and 3D printing biocomposite for preparing high-resolution dental cavities and restoration. The proposed method of applying fs-laser for dental restoration can also apply to orthopaedic treatment.

5. Conclusion

The present study proposed a HAp-based 3D printable biocomposite for direct restoration of human enamel using an integrated dual-wavelength USPL system. A precise dental cavity was prepared using an fs-laser with well-defined geometrical features. A 2D FE laser ablative model was developed to minimize the collateral damage on healthier tissue and validated with experimental results. Further, the study demonstrated the direct restoration of a laser-ablated cavity on an enamel surface using a 3D printable biocomposite. The restored enamel surface revealed no evidence of micro-cracks after photocuring and surface finish. In essence, the proposed method will pave the way to implement AI for restoring damaged enamel with a USPL and the 3D-printing technique in restorative dentistry.

Acknowledgements

The authors acknowledge the support from the European Union’s Horizon 2020 Research and Innovation (NMBP) Programme under Grant Agreement No. 953128.

Conflict of Interest

The authors declare no conflict of interest.

Data Availability Statement

The data that support the findings of this study are available from the corresponding author upon reasonable request.

Keywords

3D printing biocomposite, direct restoration, femtosecond laser, regenerative material, tissue engineering

Received: August 19, 2024
Revised: November 12, 2024
Published online:

-
- [1] T. Petrov, E. Pecheva, A. D. Walmsley, S. Dimov, *Mater. Sci. Eng. C* **2018**, *90*, 433.
- [2] L. Rapp, S. Madden, J. Brand, L. J. Walsh, H. Spallek, O. Zwitter, A. Habeb, T. R. Hirst, A. V. Rode, *Biomed. Opt. Express* **2022**, *13*, 4559.
- [3] K. P. Chang, T. W. Tsai, K. Y. Huang, C. H. Huang, S. Y. Wang, C. W. Cheng, J. K. Chen, D. Y. Tzou, *Appl. Opt.* **2013**, *52*, 6626.
- [4] M. H. Niemz, *J Dent. Res.* **1995**, *74*, 1194.
- [5] M. H. Niemz, *Laser-Tissue Interactions*, Springer, Berlin, Heidelberg **2002**, pp 45–149.
- [6] S. Loganathan, S. Santhanakrishnan, R. Bathe, M. Arunachalam, *Lasers Med. Sci.* **2019**, *34*, 693.
- [7] L. Wang, D. Wang, Y. Zhang, L. Ma, Y. Sun, P. Lv, *Lasers Surg. Med.* **2014**, *46*, 573.
- [8] S. Özüdoğru, F. Kahvecioğlu, G. Tosun, Y. Gündoğdu, H. Ş. Kılıç, *Lasers Dent. Sci.* **2021**, *5*, 199.
- [9] S. Falahatkar, A. Nouri-Borujerdi, M. Najafi, A. Mohammadzadeh, *J. Mech. Sci. Techno.* **2017**, *31*, 6085.
- [10] A. Kowalska, J. Sokolowski, K. Bociong, *Polymers* **2021**, *13*, 470.
- [11] M. S. Islam, M. Nassar, M. A. Elsayed, D. B. Jameel, T. T. Ahmad, M. M. Rahman, *Polymers* **2023**, *15*, 2121.
- [12] P. Baskaran, A. Udduttula, V. Uthirapathy, presented at *IET Nanobiotechnol.* **2018**, *12*, 138.
- [13] C. Guttridge, A. Shannon, A. O'Sullivan, K. J. O'Sullivan, L. W. O'Sullivan, *Annals of 3D Printed Medicine* **2022**, *5*, 100044.
- [14] J. Xia, Y. Li, D. Cai, X. Shi, S. Zhao, X. Yang, *BMC Oral Health* **2018**, *18*, 1.
- [15] G. Sharma, S. Loganathan, E. K. Barimah, P. Georgopoulou, E. Taylor, A. J. Scott, S. Strafford, A. Jha, *Chem. Phys. Chem.* **2024**, *25*, e202400109.
- [16] M. Lin, F. Xu, T. J. Lu, B. F. Bai, *Dental Materials* **2010**, *26*, 501.
- [17] P. Qiu, Y. Guo, L. Huang, J. Li, J. Huang, M. Wang, Z. Zhang, S. Xu, *Adv. Mater. Technol.* **2023**, *8*, 2300333.
- [18] K. H. Leitz, B. Redlingshöer, Y. Reg, A. Otto, M. Schmidt, "Metal ablation with short and ultrashort laser pulses," in *Physics Procedia*, Elsevier B.V., **2011**, pp. 230–238, <https://doi.org/10.1016/j.phpro.2011.03.128>.
- [19] A. Soori, F. Soori, F. Kowsary, S. Kasraei, *Int. J. Thermophys.* **2022**, *43*, 158.
- [20] V. B. Krapchev, C. D. Rabii, J. A. Harrington, *Laser Surg. Adv. Charact. Ther. Syst.* **1994**, *2128*, 341.
- [21] D. Fried, M. Zuerlein, J. D. B. Featherstone, W. Seka, C. Duhn, S. M. McCormack, *Appl. Surf. Sci.* **1998**, *127*, 852.
- [22] J. Cheng, W. Perrie, M. Sharp, S. P. Edwardson, N. G. Semaltianos, G. Dearden, K. G. Watkins, *Appl. Phys. A Mater. Sci. Process* **2009**, *95*, 739.
- [23] M. Sertaç Özdoğan, I. Karaokutan, M. Yıldırım, K. Aybüke Aydemir, A. Karatay, F. Aykent, *Lasers in Medical Science* **2021**, *36*, 219.
- [24] P. E. Timchenko, E. V. Timchenko, E. V. Pisareva, M. Y. Vlasov, N. A. Red'Kin, O. O. Frolov, *J. Phys. Conf. Ser.* **2017**, *784*, 012060.
- [25] J. Chen, J. Li, L. Xu, W. Hong, Y. Yang, X. Chen, *Polymers (Basel)* **2019**, *11*, 601.
- [26] https://www.chemicalbook.com/SpectrumEN_79-41-4_raman.htm (accessed: June 2024).
- [27] E. Daskalakis, A. Scott, A. Jha, *Ceram. Int.* **2023**, *49*, 24142.
- [28] S. Pramanik, A. K. Agarwal, K. N. Rai, *Trends Biomater. Artif. Organs* **2005**, *19*, 46.